 doi:10.20944/preprints202105.0784.v1

Article

New (Iso)Quinolinyl-Pyridine-2,6-dicarboxamide G-Quadruplex ligands. A Structure-Activity Relationship Study

Enrico Cadoni [1], Pedro R. Magalhães [2], Rita M. Emídio [2], Eduarda Mendes [1,3], Jorge B. Vítor [4], Josué Carvalho [5], Carla Cruz [5], Bruno L. Victor [2] and Alexandra Paulo [1,3,*]

[1] Research Institute for Medicines (iMed.ULisboa), Faculty of Pharmacy, Universidade de Lisboa, Av. Prof. Gama Pinto, 1649-003 Lisboa, Portugal;
[2] BioISI - Biosystems & Integrative Sciences Institute, Faculty of Sciences, University of Lisboa, Campo Grande, C8 bdg, 1749-016 Lisboa, Portugal
[3] Dep. of Pharmaceutical Sciences and Medicines, Faculty of Pharmacy, Universidade de Lisboa, Av. Prof. Gama Pinto, 1649-003 Lisboa, Portugal;
[4] Dep. of Pharmacy, Pharmacology and Health Technologies, Faculty of Pharmacy, Universidade de Lisboa, Av. Prof. Gama Pinto, 1649-003 Lisboa, Portugal;
[5] CICS-UBI - Centro de Investigação em Ciências da Saúde, Universidade da Beira Interior, Av. Infante D. Henrique, 6200-506, Covilhã, Portugal
* Correspondence: mapaulo@ff.ulisboa.pt;

Abstract: Quadruplex-interactive small molecules have a wide potential application, not only as drugs but also as sensors of quadruplexes structures. The purpose of this work is the synthesis of analogues of the bis-methylquinolinium-pyridine-2,6-dicarboxamide G4 ligand 360A, to identify relevant structure-activity relationships to apply to the design of other G4-interactive small molecules bearing bis-quinoline or bis-isoquinoline moieties. Thermal denaturation experiments revealed that non-methylated derivatives with a relative 1,4 position between the amide linker and the nitrogen of the quinoline ring are moderate G4 stabilizers, with a preference for the hybrid h-Telo G4. Insertion of a positive charge upon methylation of quinoline/isoquinoline nitrogen increases compounds capacity to selectively stabilize G4s compared to duplex DNA, with a preference for parallel structures. Among these, compounds having a relative 1,3-position between the charged methylquinolinium/isoquinolinium nitrogen and the amide linker are the best G4 stabilizers. More interestingly, these ligands showed different capacities to selectively block DNA polymerization in a PCR-stop assay and to induce G4 conformation switches of hybrid h-Telo G4. Molecular dynamic simulations with the parallel k-RAS G4 structure showed that the relative spatial orientation of the two methylated quinoline/isoquinoline rings determines the ligands mode and strength of binding to G4s.

Keywords: Quinoline; Isoquinoline; G-Quadruplex ligands; k-RAS; c-MYC; telomere; SAR; pyridine-dicarboxamide; molecular dynamics;

1. Introduction

With the crescent trend in incidence of cancer [1], it is becoming more and more important the need of developing effective and specific drugs to target cancer cells, for a less toxic and invasive therapy. One discussed solution can be to modulate gene expression, supported by the evidence of the role in oncogenesis played by specific proto-oncogenes. In fact, the mutations and translocations occurring within precise proto-oncogenes such as *c-MYC*[2,3], *k-RAS*[4,5], *c-KIT*[6], have been frequently reported as primary cause of cancer onset in several malignancies and for this reason they have been widely explored as potential targets [6–8].

It was demonstrated that the promoter regions of these cited genes, notably rich in guanine residues, are prone in folding into G-Quadruplexes (G4s)[9–12].These non-

 doi:10.20944/preprints202105.0784.v1

canonical structures arise when four guanines of a G-rich tract are bound together via Hoogsteen hydrogen-bonding, forming the so-called G-quartet or G-tetrad. The G4s are formed when 2 or more tetrads are stacked on top of each other, stabilized by the presence of a coordinating cation, generally potassium [13]. Beside in proto-oncogenes, several G-forming sequences have been discovered in various areas of genome, particularly the telomeric region [14]. The formation of telomeric G4 could also constitute an obstacle to the action of telomerase, the enzyme which re-synthesize the terminal part of the chromosomes and has a central role on the aging process and the developing of cancer [15,16]. The high abundance of G4-forming sequences at promoter level of genes involved in carcinogenesis, their prevalence in telomeric DNA regions, and their presence in RNA transcripts, suggests an important role of the G4 in regulation of gene expression[17–19] as well as post-transcriptional and epigenetic modulation [20], justifying the research efforts in small-molecules and oligonucleotide derivatives [21] able to induce and stabilize G4-formation, to be used as therapeutics [19,22–25]. This is of utmost importance, considering the numerous evidences that highlights G4-formation in vivo that suggests a concrete physiological role of these structures in cell development [26–28].

Among the small-molecule binders, an established family of ligands consist of the bis-quinolinyl derivatives, which display a high affinity and selectivity for G4 structures[24]. The use of a pyridine or a naphthyridine as central module, combined with a carboxamide with bond rotation impairment, forcing the ligand into a V-shape conformation, showed high benefits, maximizing the interaction with the target G4 [29–32]. A paradigmatic model of this scaffold is given by the ligand 360A (**2a**), a *N*-methylbisquinolinium-pyridine-2,6-dicarboxamide, which was shown to be a potent and selective G4-stabilizer, to bind preferentially to telomeres, *in vitro* and in human cells, and to display antiproliferative effects at low micromolar concentration in telomerase-positive human cancer cell lines [29,33]. The well-established nature as G4-binding ligand, its synthesis simplicity and affordability, led to the realization of a wide range of applications featuring this ligand or its derivatives, for instance, as alkylating and cross-linking agents for covalent targeting of G4-DNA [34,35] and G4-binding proteins [36], or the development of fluorophore-ligand conjugates for fluorescence sensing of G4-DNA [37]. Circular dichroism studies with **2a** showed that the V-shaped structure, suggested to be maintained by the formation of intramolecular hydrogen bonds between the pyridine nitrogen and the NH- carboxamide linkers, can vary in relation to the type of cations and anions present in solution [30,38]. Additionally, it was shown how the ligand is able to kick-off potassium from the telomeric G4, inducing a conformational change of the secondary structure from a hybrid structure to antiparallel [39].

Despite the numerous bis-quinoline derivatives reported as G4 ligands (reviewed in [24]), a systematic study elucidating the structure-activity relationship of the pyridine-2,6-dicarboxamide family of ligands, is still missing. In this work, we aimed to shed light on the SAR of various bis-(iso)quinolinyl-pyridine-2,6-dicarboxamides, testing their ability to efficiently stabilize G4-DNA sequences of relevant human genome regions (*k-RAS*, *c-MYC*, *h-Telo*) over double-stranded DNA sequences. Thermal denaturation experiments of the targeted sequences in presence of ligands, circular dichroism (CD)-titration experiments, biochemical assays (PCR-stop assay), as well as molecular modelling studies were used to study the influence of the carboxamide linker position in the quinoline/isoquinoline skeleton on the binding of the ligand to different G4 structures.

2. Results and discussion

2.1 Synthesis of pyridine-2,6-dicarboxamide derivatives

In a first step, a library of simple pyridine-2,6-dicarboxamides (**1b – 1h**) were prepared by reacting 2,6-pyridinedicarbonyl dichloride with the respective aminoquinoline or amino-isoquinoline in toluene, at reflux temperature (**Scheme 1, A**), according to

 doi:10.20944/preprints202105.0784.v1

previous literature reports [40,41]. Compound **1a** was prepared reacting 2-aminoquinoline with the dichloride using THF (dry) as solvent, in presence of DIPEA as a proton scavenger. The compounds were obtained pure with a yield of 50- 94%. As a following step, the *N*-methylated dicarboxamides (**2a – 2d**) were obtained making **1a-h** react with CH_3I at room temperature, from 1 to 5 days, in a solvent mixture of acetone:DMF 1:1 (**Scheme 1, B**). The pure quinolinium iodide salts were obtained as yellow precipitates upon filtration and washing with ice-cold MeOH [41], with a yield of 51-62%. The synthesis of compounds **2b-d** are here reported for the first time.

Preprints (www.preprints.org) | NOT PEER-REVIEWED | Posted: 31 May 2021 doi:10.20944/preprints202105.0784.v1

A.

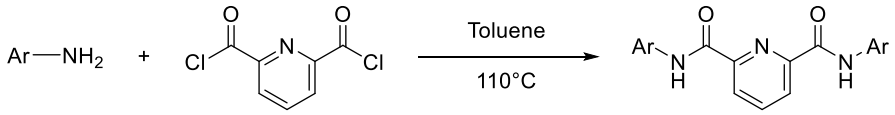

Comp.	Ar	Yield	Comp.	Ar	Yield
1a*	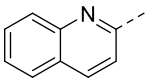	60%	**1e**	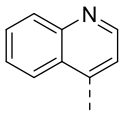	50%
1b	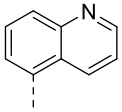	89%	**1f**	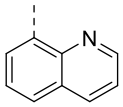	94%
1c	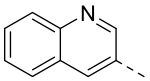	70%	**1g**	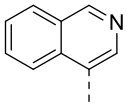	56%
1d	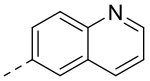	69%	**1h**	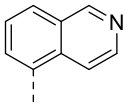	66%

B.

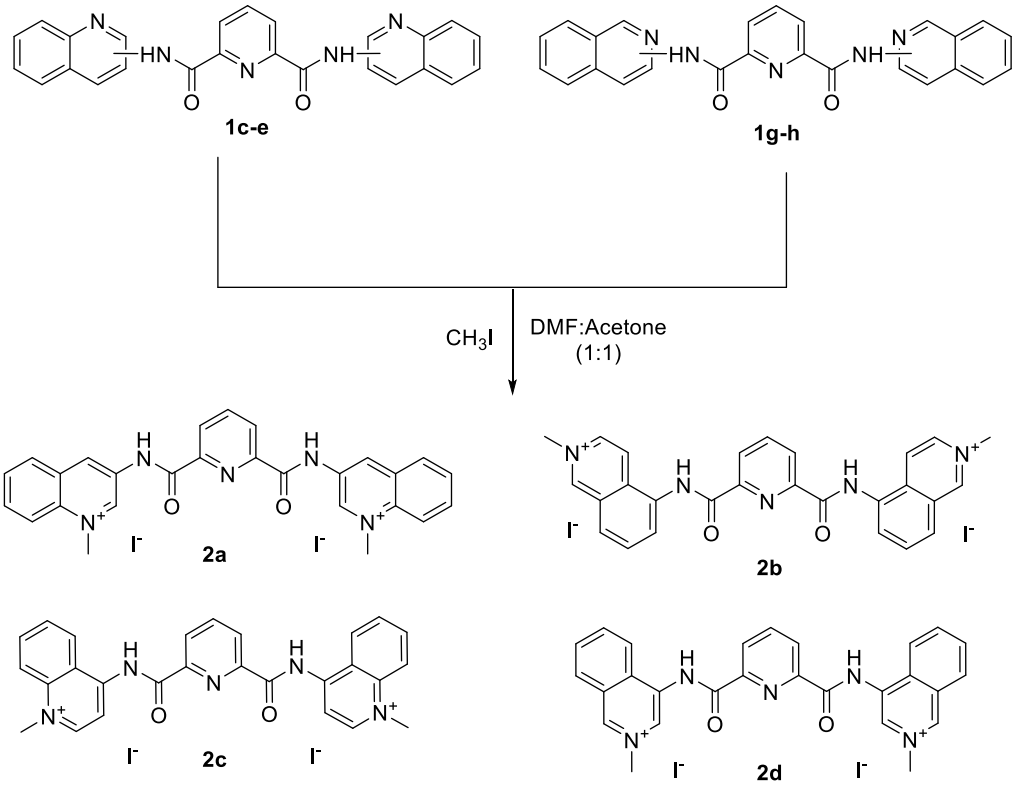

Scheme 1. Synthetic route for pyridine-2,6-dicarboxamide derivatives. **A.** Toluene, 110°C in reflux, overnight. B. CH_3I, DMF:acetone (1:1), 1-5 days, RT. * For compound **1a**, another synthetic route was followed, refluxing the mixture in THF as solvent in presence of DIPEA (please refer to material and methods section).

Preprints (www.preprints.org) | NOT PEER-REVIEWED | Posted: 31 May 2021 doi:10.20944/preprints202105.0784.v1

2.2 G4 thermal stabilization induced by compounds

As a first step to evaluate the interaction of the synthesized molecules to G4-DNA and to have an idea of the stabilization effect of these molecules, a Fluorescence Resonance Energy Transfer (FRET) melting assay was initially performed on TAMRA/FAM-labelled oligonucleotides (Please refer to Table S1 in supplementary information for the sequences). Although methylated compounds generally performed better in terms of stabilization, we found that derivatives with amide linker in positions 6 and 4 of quinoline moiety (compounds **1d** and **1e**, respectively) showed a modest stabilizing activity of promoter *k-RAS* G4 (ΔT_m = 8.0 °C) and *h-Telo* (ΔT_m = 18.0 and 11.8 °C, respectively) at a concentration of 5 μM (Table **1**). It should be noted that these compounds share the same relative 1,4 position between the amide linker and the nitrogen of the quinoline ring, which may contribute to increase binding to the G4-DNA as a result of the increased basicity of quinoline nitrogen and its consequent increased protonation at pH 7.4.

Table 1. FRET-Melting ΔT_m values for *k-RAS* G4 and *h-Telo* G4 at 0.2 μM FAM/TAMRA-labelled DNA concentration, in presence of the non-methylated dicarboxamide derivatives.

		FRET ΔT_m (°C)[a]							
	Ligand [5.0 μM]	**1a**	**1b**	**1c**	**1d**	**1e**	**1f**	**1g**	**1h**
Sequence	*k-RAS*	< 0.5	1.0 ± 0.2	3.0 ± 0.5	8.0 ± 0.2	8.0 ± 0.1	1.8 ± 0.2	< 0.5	< 0.5
	h-Telo	< 0.5	1.8 ± 0.2	2.8 ± 0.4	18.0 ± 0.3	11.8 ± 0.2	4.0 ± 0.3	< 0.5	< 0.5

[a]Experiments performed in cacodylate buffer 100 mM K^+, pH 7.4. DNA G4 melting: *k-RAS*= 49.0 ± 0.2 °C; *h-Telo* = 56.9 ± 0.2 °C

Upon insertion of a positive charge, the N-methylquinolinium derivatives tested (**2a**-**2d**), all displayed preferred stabilization of the G4 sequences compared to duplex DNA (T-loop), starting from a concentration of 1 μM, with the exception of **2a** which showed a good G4 stabilization starting at 0.1 μM, as already reported [15] (Table 2). This result suggests an increased interaction of the ligand with the negatively-charged DNA backbone, as it was reported by Pradeepkumar and co-workers for a naphtydrine-bisquinolinium derivative [31].

To further validate the stabilization induced by **2a-2d**, CD-melting assays were performed by following the G4 denaturation at the maximum CD wavelength, confirming the results previously obtained in FRET-melting assay (Table 2). Overall a concentration-dependent effect on the stabilization was observed for most ligands as higher concentrations led to a greater thermal stabilization of the G4 structure. In general, methylated compounds display a higher affinity for parallel G4, as it is shown by the higher ΔT_m values obtained in presence of *c-MYC* and *k-RAS* sequences as compared to *h-Telo*.
Regarding *c-MYC* parallel G4, all ligands beside **2b** stabilized the structure for more than 20 °C, even at low concentration as is the case of **2a**. In the case of *k-RAS* parallel G4, similar results were obtained, being **2b** the less potent stabilizer, and the remaining ligands presenting ΔT_m values greater than 20 °C. *k-RAS* was indeed the most stabilized G4 structure when compared to *c-MYC* and *h-Telo*, being the latter the structure for which the ligand-induced thermal stabilization was less evident.

Preprints (www.preprints.org) | NOT PEER-REVIEWED | Posted: 31 May 2021 doi:10.20944/preprints202105.0784.v1

Table 2. Melting temperature variations (ΔT_m) values for the tested sequences, obtained via FRET-melting assay (top) and CD-melting assay (bottom), for the methylated dicarboxamide derivatives.

FRET ΔT_m (°C)[a]

Ligand C (μM)		2a			2b			2c			2d		
		0.1	**0.3**	**0.5**	**1.0**	**3.0**	**5.0**	**1.0**	**3.0**	**5.0**	**1.0**	**3.0**	**5.0**
Sequence	*k-RAS*	14.0 ±0.3	32.8 ±0.2	35.6±0.3	4.0 ±0.2	9.0 ±0.1	11.1 ±0.2	11.8 ±0.2	16.6 ±0.2	18.2 ±0.2	15.0 ±0.2	23.1 ±0.1	26.1 ±0.2
	h-Telo	1.1 ±0.2	13.2 ±0.2	18.8 ±0.3	2.3 ±0.1	8.0 ±0.3	10.1 ±0.1	9.8 ±0.2	13.1 ±0.1	14.7 ±0.1	15.1 ±0.1	20.1 ±0.2	22.7 ±0.2
	t-Loop	2.0 ±0.1	5.6 ±0.1	6.5 ±0.1	< 0.5	< 0.5	1.8 ±0.2	<0.5	0.7 ±0.1	1.2 ±0.1	<0.5	1.5 ±0.1	2.5 ±0.1

[a]Experiments performed in cacodylate buffer 100 mM K^+, pH 7.4. G4 DNA melting: *k-RAS*= 49.0 ± 0.2 °C; *h-Telo* = 56.9 ± 0.2 °C; *t-Loop* = 53.2 ± 1.0 °C.

CD ΔT_m (°C)[b]

Ligand (eq)		2a				2b				2c				2d			
		1.0	5.0	10	25	1.0	5.0	10	25	1.0	5.0	10	25	1.0	5.0	10	25
Sequence	*k-RAS*	>40	>40	>40	**P**	3.0 ± 0.2	12.2 ± 0.2	15.1 ± 0.2	**P**	13.8 ± 0.3	35.9 ± 0.1	37.1 ± 0.1	>40	12.6 ± 0.4	>40	>40	>40
	h-Telo	3.5 ± 0.1	12.2 ± 0.3	Topology Change		1.7 ± 0.2	4.4 ± 0.2	6.9 ± 0.2	9.2 ± 0.2	3.3 ± 0.1	9.0 ± 0.1	9.0 ± 0.2	10.8 ± 0.3	6.8 ± 0.2	14.9 ± 0.2	19.8 ± 0.4	27.0 ± 1.3
	c-MYC	35.7 ± 1.3	>40	>40	>40	2.7 ± 0.2	5.3 ± 0.1	7.0 ± 0.2	9.7 ± 0.2	8.0 ± 0.2	24.1 ± 0.1	25.0 ± 0.1	29.4 ± 0.1	11.8 ± 0.2	31.2 ± 0.2	34.4 ± 0.2	>40

[b]Experiments performed in 20 mM potassium phosphate, pH 7.2, following the CD λ_{max} for each sequence: 265nm (*k-RAS* and *c-MYC*); 290 nm (*h-Telo*); 264 nm. DNA melting: *k-RAS*= 48.3 ± 0.2 °C; *h-Telo* = 59.6 ± 0.9 °C; *c-MYC* = 50.4 ± 1.9 °C. **P**= DNA precipitation.

Preprints (www.preprints.org) | NOT PEER-REVIEWED | Posted: 31 May 2021 doi:10.20944/preprints202105.0784.v1

Overall, both techniques indicate for all G4-DNA structures, an induced thermal stabilization activity trend of **2a** > **2d** > **2c** > **2b**. Also, the relative position of the quinoline nitrogen and the amide -NH, seems to play a role in quadruplex stabilization. The two most active compounds (**2a** and **2d**) show the common structural feature of having a relative 1,3-position between the charged methyl-quinolinium/isoquinolinium nitrogen and the amide linker.

Finally, the selectivity of methylated compounds for G4-DNA over double-stranded (ds) DNA, was assessed. For doing so, T_m of the FAM/TAMRA-labelled G4 sequence of *k-RAS* complexed with the ligands, was recorded in presence of increasing concentrations of competing dsDNA, up to 125-fold. For all the tested compounds, the presence of the competing DNA showed neglectable destabilization of the G4-ligand complex, thus confirming the high selectivity of the compounds for G4-DNA (Figure 1).

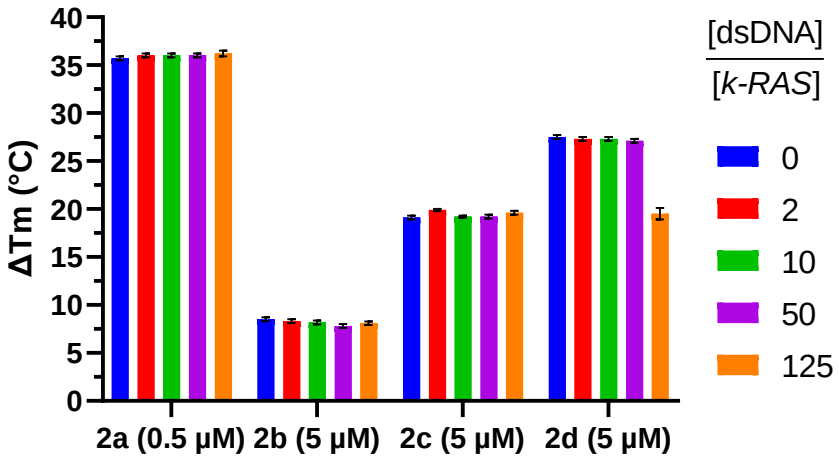

Figure 1. FRET-melting competition assay results for compounds **2a-d** at 0.5 μM (**2a**) and 5 μM (**2b-d**) complexed with *k-RAS* (0.2 μM), challenged with increasing concentrations of non-labeled 26ds DNA (dsDNA)(0.4 to 25 μM) competitor. Experiment performed in cacodylate buffer (100 mM K^+, pH 7.4).

2.3. G4 conformational changes induced by G4 ligands ***2a-2d***

To retrieve additional information about the binding of the best ligands to G4s, we decided to perform CD-titration experiments. Sequence *h-Telo* folds into a hybrid-type G4 structure in K^+ solution as suggested by its characteristic CD signature containing a positive band at 290 nm, a shoulder peak at 265 nm and a weak negative at around 240 nm (Figure 2). CD-titration experiments on *h-Telo* suggest that ligand **2a** is able to induce conformational switch upon binding to the target, switching from a hybrid (3+1) topology to a parallel topology (appearance of the typical signature λ_{max} = 264 nm) (Figure 2A). These results contrast with what has been reported previously by Marchand and colleagues [39] where **2a** was suggested to convert *h-Telo* from a hybrid-type to an antiparallel topology in K^+ solution. However, the sequence used was longer (24 bp) than that used in our study (21 bp) and the potassium concentration was lower (1 mM K^+). It is well known that sequence composition and length, and salt concentration strongly affect the G4 topology of telomeric G4s [42–44]. Surprisingly, this behavior was not preserved by the other methylated derivatives, as even in large ligand excess, the characteristic signature of hybrid G4 (λ_{max} = 290 nm) is maintained. Ligands **2b** and **2c** seem to interact with *h-Telo* as suggested by the slight ellipticity alteration, particularly around 260 nm, but the overall topology seems to be maintained (Figures 2B and 2C). In the case of ligand **2d** (Figure 2D), the G4

Preprints (www.preprints.org) | NOT PEER-REVIEWED | Posted: 31 May 2021 doi:10.20944/preprints202105.0784.v1

topology seems to be interconverted into an antiparallel structure as suggested by the strong negative band at 260 nm and a weak positive at around 240 nm following ligand titration.

In the case of *c-MYC*, it folds into a typical parallel G4 as shown by the positive band at 260 nm and negative band at 240 nm (Figure S1). Upon titration with the ligands, only a minor ellipticity variation was observed, suggesting ligand binding without affecting or interconverting the G4 structure. Indeed, *c-MYC* parallel G4 structure is very stable in the K^+ conditions used and one of the most stable G4s studied [45]. *k-RAS* on its hand, folds into a parallel-stranded G4 structure similarly to *c-MYC* (Figure S2), but upon titration with the ligands, a significant decrease in the ellipticity could be observed, particularly in the case of **2b**, **2c** and **2d** (Figures S2B, S2C and S2D). This signal decrease was accompanied by the appearance of a CD band around 295 nm that suggests structural interconversion and possibly the formation of a hybrid G4 topology.

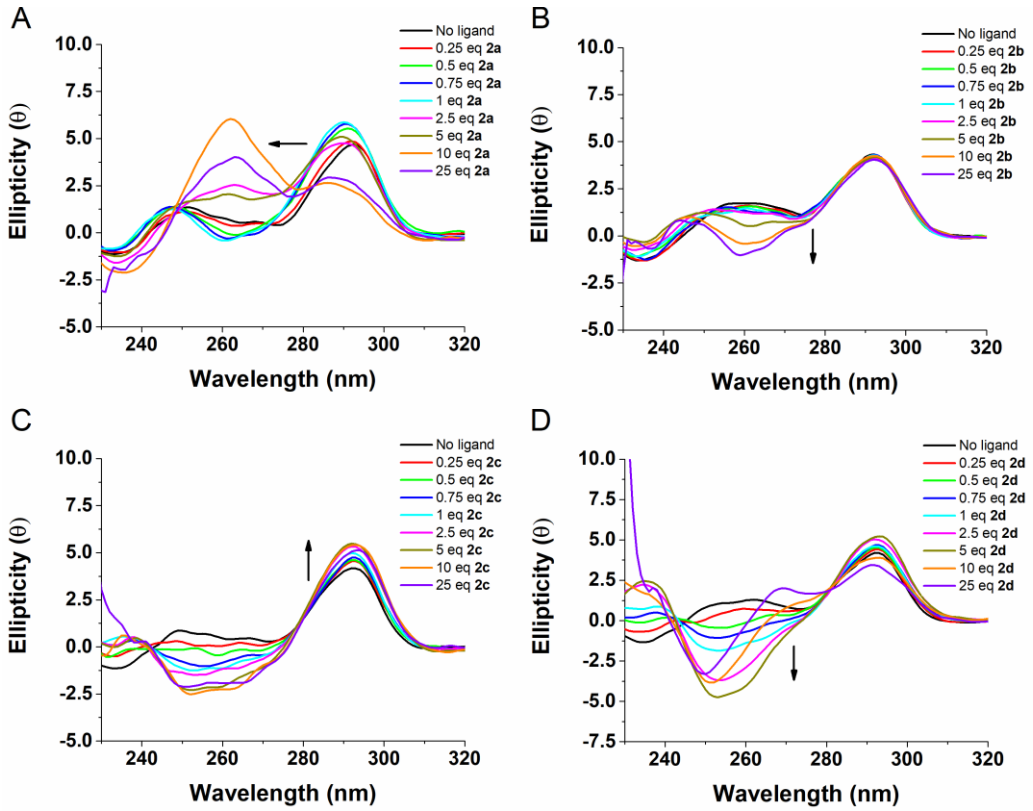

Figure 2. CD titration of *h-Telo* in presence of increasing equivalents (0-25) of compound 2a (A), 2b (B), 2c (C), 2d (D), at a concentration of 10 μM, performed in 20 mM lithium cacodylate containing 10 mM KCl and 90 mM LiCl.

2.4 Taq polymerase inhibition by G4-ligands.

To evaluate the ability of the compounds in blocking DNA replication upon G4-stabilization, a polymerase chain reaction (PCR)-stop assay using the G4-forming 27-nucleotide sequence (Pu27) present in the wild-type promoter region of the *c-MYC* oncogene (see sequences in Table S3) was performed according with the methodology previously reported [46]. The test is commonly used to evaluate the concentration of ligand necessary to induce the more stable loop-isomer involving G-tracts 2-3-4-5 and block DNA polymerase activity by inhibiting DNA hybridization at G-tract 5 [46]. Consistently with FRET-melting experiments, the non-methylated compounds did not show a significant activity up to 50 μM concentration, even in case of the best stabilizers of the series, **1d** and **1e**, (Figure S3A). On the other hand, and further confirming the results obtained with FRET

Preprints (www.preprints.org) | NOT PEER-REVIEWED | Posted: 31 May 2021 doi:10.20944/preprints202105.0784.v1

and CD-melting analyses, the two more potent methylated compounds, **2a** and **2d,** proved to be able to block polymerase activity at a concentration of 5 and 10 μM, respectively (Figure 3A). In contrast, the least stabilizing ligands **2b** and **2c**, inducing a low/moderate ΔT_m in both FRET and CD melting assays, did not display any activity up to a concentration of 50 μM, in line to what was obtained for the non-methylated **1d**-**1e**. When a mutated sequence at G-tract 3 is used in place of native Pu27 (G13,14→ A mutation), the primer elongation is maintained in the presence of **2d**, even at high excess of ligand (Figure 3B) similarly to that observed for the related compound 307A [47], thus confirming that the polymerase blockade mechanism is ascribed to G4-stabilization rather than to non-specific interactions of the ligand with the DNA primer or with the enzyme, as it seems to be the case of ligand **2a** (Figure 3B and S3B). Another possibility to justify these results is the ligand **2a** to be also able to induce the formation of the less stable G4 loop isomer involving G-tracts 1-2-4-5 and in this way block hybridization of primers and subsequent replication by polymerase.

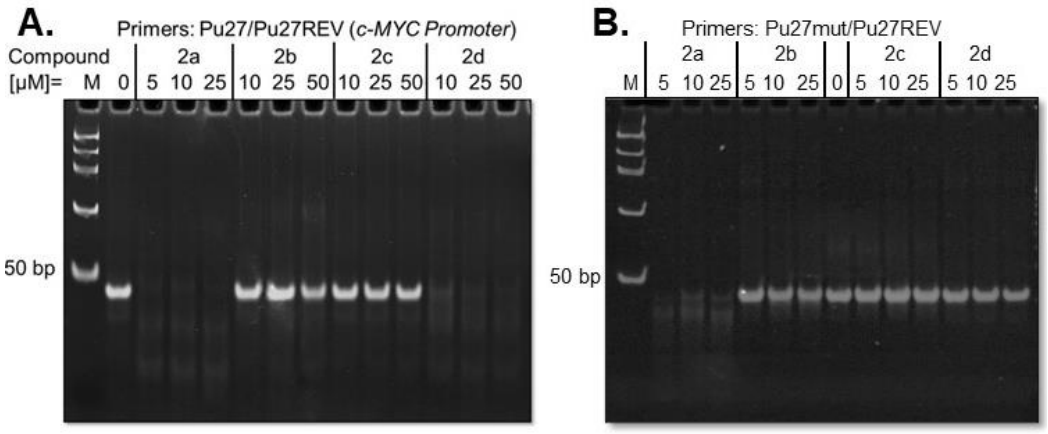

Figure 3. Polyacrylamide gels stained with ethidium bromide showing the effect of compounds on polymerization of DNA constructs A) containing the *c-MYC* promoter wild-type sequence (Pu27) or B) with a mutated *c-MYC* promoter sequence (Pu27mut). In absence of compound (0 μM), the 43 bp PCR product is formed. M: PCR molecular weight marker.

2.4 Molecular Dynamics

To structurally characterize the interaction of **2a**, **2b**, **2c** and **2d** ligands with the *k-RAS* molecule, we have performed long replicate MD simulations on a 1:1 ratio. In each replicate simulation, the compounds were randomly placed around the *k-RAS* parallel structure (PDB ID: PDB 5i2v). This was done to assure that each simulation was unbiased from any other replicate simulation. The initial 250 ns were not considered for the data analysis of the simulations, since only after this simulation time the complexes reached an equilibrium conformational state (Figure S4).

To evaluate the convergence of the conformational space sampled by the ligand:*k-RAS* complex during the MD simulations of each system, we built root mean square deviation (RMSD) histograms calculated from the production trajectories. As can be seen in Figure **4**, where we have the probability density of the conformations visited during the MD simulations for each compound, compound **2a** adopts a lower range of conformations, when compared to all the other compounds. While for compound **2a** we can observe one single peak, indicating a highly populated conformation, in compounds **2b**, **2c** and **2d** at least two highly populated peaks of conformations can be identified. This observation clearly indicates that the convergence of the interaction conformations adopted by compound **2a** is much higher, when compared to all the other compounds.

Preprints (www.preprints.org) | NOT PEER-REVIEWED | Posted: 31 May 2021 doi:10.20944/preprints202105.0784.v1

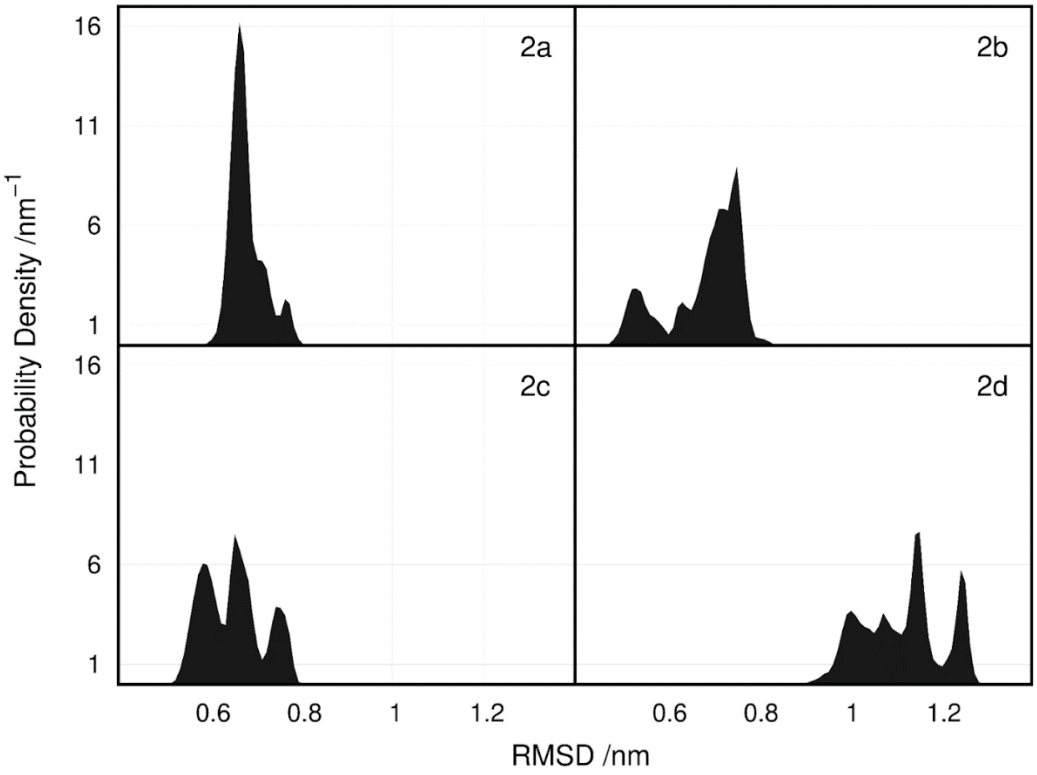

Figure 4. Probability density of the RMSD calculated for all replicate simulations of the different ligands+*k-RAS* complexes. RMSD values were calculated taking as reference, the initial conformation of the complex of the first replicate for each simulated system.

To identify the preferred interaction configurations between the different compounds and *k-RAS* G4, the number of contacts between the two partners was calculated. Results are presented in Figure 5 and S6-S9, where *k-RAS* residues were colored accordingly. Regarding compound **2a**, we can see that both the top and bottom regions of the *k-RAS* molecule, close to its 3′ and 5′ terminal, respectively, are the regions showing highest number of contacts. By visually inspecting the MD trajectories of the different replicates for this compound, we could verify that in replicates 1, 2, 4 and 5, compound **2a** binds the *k-RAS* at its top, closer to the 3′ terminal, while in replicate 3, the most prevalent configuration shows an interaction of the ligand at the bottom surface, close to the 5′ terminal. Overall, adenine 1, guanine 6 and 11 and adenine 17 showed to be the preferred spots of interaction for this compound. Regarding compound **2b**, we can also clearly identify that the region of *k-RAS* with more interactions was the side loop groove close to adenine 14 and 15. The visual inspection of the trajectories of the different replicate MD simulations indicates that in replicates 2, 3 and 4, compound **2b** interacts preferably with this region of the DNA molecule. This interaction configuration is quite distinct from what was observed in replicate 1 and 5, where the compound **2b** binds respectively the top and bottom of the quadruplex, with the compounds establishing contacts with the guanine tetrad of *k-RAS*. In what concerns compound **2c**, both the top and the bottom regions of k-RAS G4 are the regions with a higher number of contacts. The visual inspection of the different replicate MD simulations indicates that in replicates 1 and 2, compound **2c** binds to the bottom of the G4, while in replicates 4 and 5, the ligand preferably binds at its top. In replicate 3, we could observe that compound **2c** binds also at the side region of the G4 close to residues 12 and 17. Finally, regarding compound **2d**, we clearly see that the preferred region of interaction with *k-RAS* G4 is the bottom region close to the 5′ terminal. The visual inspection of the different trajectories indicates that in replicates 3 and 5 compound **2d** preferably binds the side region of *k-RAS* (between residues 15 and 19), in replicates 2 and 4 the interaction is mostly

Preprints (www.preprints.org) | NOT PEER-REVIEWED | Posted: 31 May 2021 doi:10.20944/preprints202105.0784.v1

done at the bottom region close to the 5′ terminal, while in replicate 1 the preference for interactions is observed at the top of *k-RAS* G4, close to the 3′ terminal. Overall, these results confirm the conclusions previously taken from the analysis of the RMSD histograms, where compound **2a** shows a higher convergence of pose interactions to *k-RAS* when compared to all the other tested compounds.

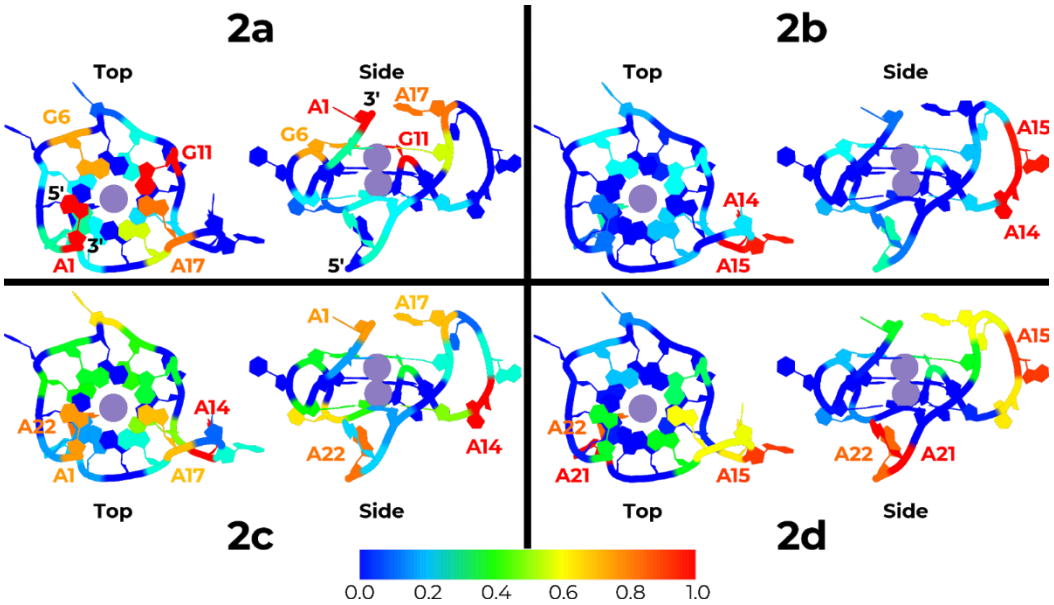

Figure 5. Cartoon representation of the structure of *k-RAS* (top-view on left and side-view on the right) colored according to the normalized number of contacts determined from all the MD simulations (red to dark blue representing the highest number of contacts to the lowest number of contacts).

From the previous analysis it is however difficult to identify a specific binding pose that could be seen as a representative of interaction between each one of the compounds and *k-RAS* G4. Therefore, we have analyzed the binding free energy of each compound throughout all the replicate simulations to identify a representative lowest binding affinity pose. To achieve this goal, we performed MM/PBSA calculations every 5 nanoseconds of simulation for all replicates and systems and identified the part of the trajectory of the replicate where a lower value for the interaction of the compound and the *k-RAS* G4 was observed. Ultimately, from these sets of conformations we selected a representative of the interaction between *k-RAS* and each compound (Figure 6 and S5).

In the selected lowest binding energy representative conformation of compound **2a** with *k-RAS* G4 we can see that the compound stacks in a planar configuration at the bottom region of the G4, close to the 5′ terminal. A perfect stack between the pyridine, the two quinoline groups and the guanine rich core of the parallel G4 is achieved. Interestingly, both the positively charged N-methylated groups in the two quinolines are facing the outward region of the core of the G4, directed to the negatively charged phosphate groups, evidencing a strong electrostatic attractive effect (see Table 3). Additionally, it is also possible to observe that one of the quinolines is double stabilized by the aromatic rings of guanine 20 and adenine 21, in an intercalating aromatic configuration that restrains the movements of this group, and consequently stabilizes the entire molecule on this conformation.

The previously described interaction observed in compound **2a** is completely distinct from the interaction observed in the representative lowest binding affinity conformation of compound **2b** with *k-RAS*. As can be seen in figure 6, compound **2b** directly interacts on a side groove of *k-RAS* between adenine 15 and guanine 19. In this conformation, the pyridine group of the compound stacks with adenine 15, with both the quinolines showing a 90º rotation of the aromatic groups in respect to the plane of the pyridine group. This

Preprints (www.preprints.org) | NOT PEER-REVIEWED | Posted: 31 May 2021 doi:10.20944/preprints202105.0784.v1

configuration allows for one of the quinolines to stack with the aromatic region of adenine 14 and with the N-methylated group facing the phosphorus of guanine 20. The other quinoline faces the solvent, exposing the N-methylated group to the environment water molecules. This configuration, although showing a good binding free energy to *k-RAS* (see Table I), is in a completely different interaction configuration when compared to compound **2a**. Moreover, it is also possible to find interaction configurations of compound **2b** in a similar configuration to the one previously described for compound **2a** (stacked at the top and bottom regions of *k-RAS).* However, these configurations are of much higher binding free energy, which could be correlated with its lower ability to stabilize *k-RAS*.
Regarding the representative lowest binding affinity configuration for compound **2c** (figure 6) we can see that, similarly to compound **2a**, this compound stacks at the bottom of the *k-RAS* G4. Both the pyridine and quinoline groups of this compound are stacked with the central guanine tetrads. Additionally, the positive N-methylated groups in quinolines are also facing the phosphate backbone of G4, establishing strong favorable electrostatic interactions (Table 3). However, while compound **2a** shows a full planar interaction configuration at top of the G4 molecule, in compound **2c** only one quinoline is fully stacked with adenine 21, while the other quinoline evidences a twisted conformation which ultimately results in a less stable configuration when compared to compound **2a**.
Finally, in what concerns compound **2d**, similarly to what was observed for compounds **2a** and **2c**, the lowest binding affinity representative conformation is found stacking on the top of the *k-RAS* G4 in a very similar configuration as the one adopted by compound **2c**. The major difference observed from these two compounds comes from the more planar conformation with the guanine-rich core of *k-RAS*, which is further stabilized by stacking with adenine 17. Additionally, both the N-methylated groups seem to adjust in order to assure that a favorable electrostatic interaction with the negatively charged phosphate groups of the DNA backbone is achieved. This interaction configuration seems to allow compound **2d** to interact and stabilize *k-RAS* to a higher extent when compared to compound **2c.**

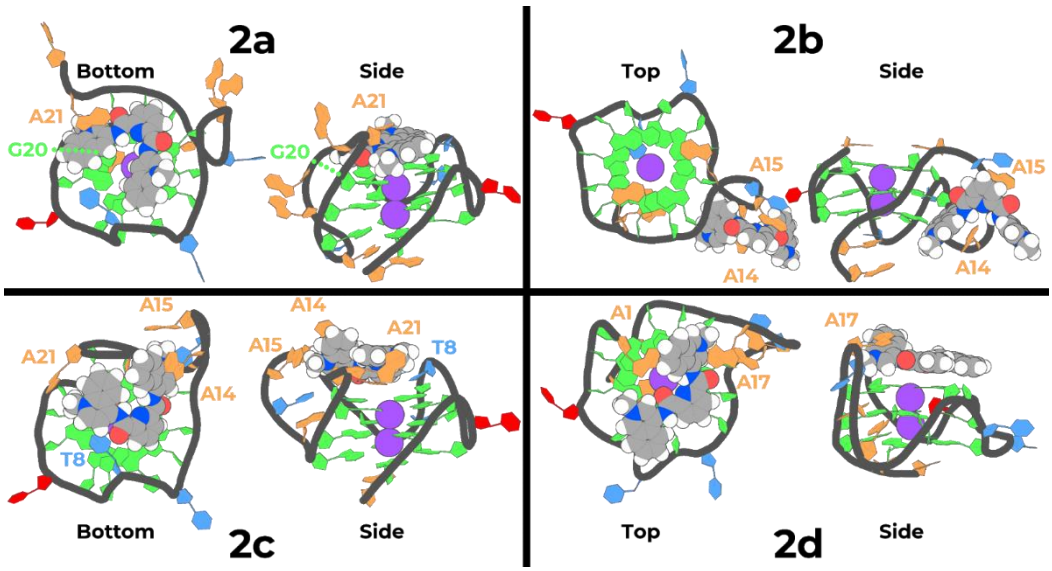

Figure 6. Snapshots of the representative lowest binding energy pose of each compound to parallel *k-RAS* G4 (top or bottom views on the left and side views on the right). The backbone of *k-RAS* G4 molecule is represented as black cartoon, and all the side-chains of the pairs of bases are differently colored with filled lines and sticks: guanines are colored in green, adenines in orange, thymines in blue and cytosines in red.

To try to correlate the binding free energies of the representative configurations of the different compounds with the experimental melting temperature assay results, we have

Preprints (www.preprints.org) | NOT PEER-REVIEWED | Posted: 31 May 2021 doi:10.20944/preprints202105.0784.v1

calculated the average binding free energy of the different compounds with the 50 more similar configurations to the previously analyzed representative solutions (based on RMSD differences). As can be seen in Table 3, compound **2b** stands out as the one showing a higher binding free energy to the *k-RAS* G4. However, one should mention that the interaction configurations showing these binding free energy values correspond to quite different configurations in respect to the ones observed for all the other compounds.

Another fact that is possible to identify from the analysis of Table 3, is that the electrostatic energies are the forces that most contribute to the overall binding free energies, which most probably come from the previously described electrostatic interactions observed between the N-methylated groups of the quinolines and the backbone phosphates of the DNA. Overall, the representative interaction configurations identified from the MD simulations for compounds **2a**, **2c**, and **2d** show a clear stacking of the pyridine and quinoline groups with the guanine tetrad at the core of *k-RAS* G4, with the positive N-methylated groups of the quinolines interacting with the negative G4-DNA phosphates. The small conformational differences observed between the different compounds with G4, which consequently are responsible for the determined differences in the binding free energies, seem to come from the degree of achieved planarity between the aromatic groups. Except for compound **2b**, the binding results obtained can directly be correlated with the results from the melting temperature assays previously described, reporting compound **2a** as the one with a higher ability to stabilize *k-RAS* G4 when compared to compounds **2d** and **2c**, respectively. However, one should recall that binding free energies only evaluate the binding and should not be directly correlated with the stabilization effect of the different compounds on the full G4. Therefore, despite we were able to get a good correlation between the binding affinities and the melting temperature assays for compounds **2a**, **2c** and **2d**, the results obtained for compound **2b** evidence the need for a careful analysis between the determined binding affinity results and the overall stabilization of the G4 determined by the temperature melting assays.

Table 3. Average binding free energy of the representative configurations of the different compounds with the *k*-RAS G4. 50 snapshots were used in the calculations.

Ligand	Average Binding Free energy (kj/mol)	Van der Waals energy (kj/mol)	Electrostatic energy (kj/mol)	Polar solvation energy (kj/mol)	SASA energy (kj/mol)
2a	-207 ± 8	-240 ± 6	-560 ± 4	612 ± 13	-19 ± 1
2b	-215 ± 14	-220 ± 5	-518 ± 4	543 ± 17	-19 ± 1
2c	-171 ± 8	-248 ± 8	-553 ± 4	649 ± 9	-19 ± 1
2d	-203 ± 7	-217 ± 7	-521 ± 5	551 ± 14	-17± 1

3. Conclusions

Bis-quinoline dicarboxamides, particularly those N-methylated, are known to be potent G4 stabilizers. In the past, the influence of the central module on compounds capacity to bind and stabilize DNA G4s was well studied [24], but in all these studies only three linking positions of carboxamide group to quinoline ring were explored: positions 2 (pyridostatin and analogs) ,[48] 3 (e.g. 360A) and 6 (e.g. 307A). [15]. In this work we synthesized new bis-quinolinyl/isoquinolinyl-2,6-pyridine dicarboxamides, to study the influence of the position of carboxamide linker in the quinoline/isoquinoline rings on the molecular geometry and electronic distribution, and how these parameters impact on compounds' selective binding and stabilization of G4s of different topologies.

 doi:10.20944/preprints202105.0784.v1

Following a simple synthetic protocol, we were able to successfully obtain six bis-quinolinyl and two bis-isoquinolinyl derivatives, compounds **1a-h**, with yields of 50-94% (Scheme 1). FRET melting experiments revealed that from these, only compounds with the amide-NH linked to positions 6 (**1d**) and 4 (**1e**), that is, with a relative 1,4-position between this group and the quinoline nitrogen, showed moderate G4 stabilizing capacity, with a preference for the hybrid *h-Telo* G4. Similarly, it was shown that the presence of a 4-amine group in the quinoline ring of N^2,N^6-di(quinolin-6-yl)pyridine-2,6-dicarboxamide leads to a G4 ligand as potent as the methylated counterpart [15]. This may be explained by an increased fraction of protonated quinolines nitrogens due to the electron donator character of amine/amide-NH in a 1,4-relative position. Upon methylation of the quinoline/isoquinoline nitrogens, all compounds became much better G4 stabilizers (**1c** vs **2a**, **1e** vs **2c**, **1g** vs **2d** and **1h** vs **2b**), showing a relative potency trend of **2a** > **2d** > **2c** > **2b**, as determined by FRET and CD-melting assays, and a general preference for parallel G4 structures. In addition, FRET-melting competition assays showed that ligands **2a-2d** are selective to G4s up to around 100-fold concentration of double strand DNA. We have also studied by CD the capacity of **2a-2d** to induce a G4 topology switch and block polymerase activity in a PCR-stop assay. Compound **2a** was able to switch the hybrid 21-nt *hTelo* G4 to a parallel topology, whereas **2d** induced an interconversion of this G4 from hybrid to an antiparallel topology. Both compounds were also able to inhibit DNA-polymerization of the primer with the G4-forming sequence present in *c-MYC* promoter, being **2d** more selective, since **2a** also inhibited the polymerization of the mutated sequence.

To understand the molecular features of compounds **2a-2d** behind the observed significant differences between these analogs on G4 stabilization, we performed molecular dynamic simulations using the parallel k-RAS22 G4 structure determined by NMR (PDB ID 5i2v). Figure 6 shows that best G4 stabilizers **2a**, **2c** and **2d** bind to the G-quartet through π-π stacking between the quinoline/isoquinoline and pyridine rings of the ligand and the guanines of the G4, as well as through electrostatic interactions between the cationic quinoline/isoquinoline nitrogens and the G4 phosphate backbone. Moreover, position of the methyl groups in relation to the pyridine-2,6-dicarboxamide central module is determinant for the overall geometry of the ligand. Best G4 stabilizer (**2a**) can adopt an almost planar configuration, which optimizes the π-π stacking interactions, whereas worst G4 stabilizer (the isoquinoline derivative **2b**) interacts preferentially with the groove of a loop of the G4, in a complete twisted configuration.
Quadruplex-interactive small molecules have a wide potential application, not only as drugs but also as sensors of quadruplexes structures. With this work we increased the portfolio of G4 ligands of the pyridine-2,6-dicarboxamide family and showed that introduction of a electron donator group in position 4 of que quinoline ring increases G4 stabilization capacity of the ligands, whereas upon N-methylation of the quinoline or isoquinoline rings, the relative spatial orientation of the two quinoline/isoquinoline rings determines the ligands mode and strength of binding to G4s. Overall, we report here new isomers of the potent G4 ligand 360A (**2a**) presenting different strengths and modes of binding to G4s, which maybe important when seeking for selectivity. This was here shown by the new bis-methyl-isoquinolinium derivative **2d** which is less potent G4 stabilizer than **2a** but is more selective than this latter one in blocking DNA polymerization upon stabilization of the 2-3-4-5 G4 loop-isomer of the *c-MYC* promoter sequence (Figure 3). Knowing the structural features of these molecules governing the binding to G4 structures is crucial for the rational development of better therapeutics and more selective G4 sensors.

4. Materials and Methods

4.1 Synthesis of compounds

4.1.1 General procedure A for synthesis of bis-quinolinyl/isoquinolinyl-pyridine-2,6-dicarboxamides (**1b-1h**).

Preprints (www.preprints.org) | NOT PEER-REVIEWED | Posted: 31 May 2021 doi:10.20944/preprints202105.0784.v1

In a round-bottom flask, a mixture of aminoquinoline/amino-isoquinoline (70 mg, 0.60 mmol) and pyridine-2,6-dicarbonyl-dichloride (50 mg, 0.245 mmol) was refluxed overnight in 2.0 ml of freshly-dried toluene. The resulting precipitate was recovered by suction filtration, washed with acetone and a 5% aqueous solution of $NaHCO_3$, to obtain the titled compound (**1b-1h**) as a white powder with a yield of 50-95%.

N^2,N^6-di(quinolin-2-yl)pyridine-2,6-dicarboxamide (**1a**). 2-aminoquinoline (77.75 mg, 0.539 mmol) was dissolved in 3 ml of THF and 93.92 µL of DIPEA (0.539 mmol) added to the mixture. Pyridine-2,6-dicarbonyl-dichloride (50 mg, 0.245 mmol) was finally added to the solution refluxed for 24H. The solvent was then removed in vacuum and the product purified by flash chromatography (100 Hexane to 3:7 Hexane/EtOAc), to give a light brown powder in a yield of 60%. **^{1}H NMR** ($CDCl_3$) δ 11.27 (s, 2H), 8.63 (d, J = 8.7 Hz, 2H), 8.45 (d, J = 7.8 Hz, 2H), 8.18 (d, J = 9.0 Hz, 2H), 8.08 (t, J = 7.8 Hz, 1H), 7.90 (d, J = 8.4 Hz, 2H), 7.74 (d, J = 7.9 Hz, 2H), 7.64 (t, J = 7.7 Hz, 2H), 7.42 (t, J = 7.5 Hz, 2H). **^{13}C NMR** ($CDCl_3$) δ 162.18, 150.87, 148.54, 146.26, 139.50, 139.00, 130.20, 127.60, 127.44, 126.38, 125.96, 125.51, 114.50. **ESI-MS m/z** (100%), 420.3 ([M+H]$^+$).

N^2,N^6-di(quinolin-5-yl)pyridine-2,6-dicarboxamide (**1b**). The title compound was synthesized following the general synthetic procedure A, reacting pyridine-2,6-dicarbonyl-dichloride with 5-aminoquinoline, with a final yield of 89%. **^{1}H NMR** (DMSO-d6) δ 11.48 (s, 2H, NH), 8.97 (d, J = 2.4 Hz, 2H), 8.57 - 8.43 (m, 4H), 8.37 (dd, J=7.2, 7.8 Hz, 1H), 8.02 (d, J = 8.1 Hz, 2H), 7.92 – 7.77 (m, 4H), 7.64 (dd, J = 9.0, 6.0 Hz, 2H). **^{13}C NMR** (DMSO-d6) δ 163.21, 151.32, 148.96, 148.59, 140.69, 133.76, 132.75, 129.59, 128.19, 125.96, 125.00, 124.96, 121.92. **ESI-MS m/z** (100%), 420.3 ([M+H]$^+$).

N^2,N^6-di(quinolin-3-yl)pyridine-2,6-dicarboxamide (1c). The title compound was synthesized following the general synthetic procedure A, reacting pyridine-2,6-dicarbonyl-dichloride with 3-aminoquinoline, with a final yield of 70%. **^{1}H NMR** (DMSO-d6) δ 9.39 (d, J = 2.5 Hz, 2H), 8.98 (d, J = 2.5 Hz, 2H), 8.47 (d, J = 7.6 Hz, 2H), 8.36 (dd, J = 7.8, 6.9 Hz, 1H), 8.03 (d, J = 8.1 Hz, 4H), 7.71 (td, J = 9.0, 1,2 Hz, 2H), 7.63 (td, J = 9.0, 1.0 Hz, 2H). **^{13}C NMR** (DMSO-d6) δ 162.94, 148.93, 146.55, 145.12, 140.72, 132.41, 129.11, 128.87, 128.40, 128.16, 127.64, 126.12, 124.88. **ESI-MS m/z** (100%), 420.3 ([M+H]$^+$).

N^2,N^6-di(quinolin-6-yl)pyridine-2,6-dicarboxamide (**1d**). The title compound was synthesized following the general synthetic procedure A, reacting pyridine-2,6-dicarbonyl-dichloride with 6-aminoquinoline, with a final yield of 69%. **^{1}H NMR** (DMSO-d6) δ 11.39 (s, 2H, NH), 8.86 (dd, J = 4.2, 1.6 Hz, 2H), 8.73 (d, J = 2.2 Hz, 2H), 8.49 (d, 2H), 8.43 (dd, J = 7.6, 2.3 Hz, 2H), 8.37 (t, J = 8.6, 6.8 Hz, 1H), 8.26 (dd, J = 9.1, 2.3 Hz, 2H), 8.13 (d, J = 9.1 Hz, 2H), 7.56 (dd, J = 8.3, 4.2 Hz, 2H). **^{13}C NMR** (DMSO-d6) δ 162.53, 150.03, 149.15, 145.48, 140.68, 136.49, 136.40, 129.87, 128.69, 126.12, 125.40, 122.44, 117.72. **ESIMS m/z** (100%), 420.3 ([M+H]+).

N^2,N^6-di(quinolin-4-yl)pyridine-2,6-dicarboxamide (**1e**). The title compound was synthesized following the general synthetic procedure A, reacting pyridine-2,6-dicarbonyl-dichloride with 4-aminoquinoline with a final yield of 50%. **^{1}H NMR** (DMSO-d6) δ 11.59 (s, 2H, NH), 8.98 (d, J = 4.9 Hz, 2H), 8.53 (d, J = 7.5 Hz, 2H), 8.46- 8.35 (m, 3H), 8.10 (d, J = 8.5 Hz, 2H), 8.01 (d, J = 4.9 Hz, 2H), 7.86 (td, J = 7.8, 1.4 Hz, 2H), 7.75 (td, J = 7.7, 1.4 Hz, 2H). **^{13}C NMR** (DMSO-d6) δ 163.92, 152.21, 150.16, 149.71, 142.34, 141.83, 131.31, 130.73, 127.82, 127.53, 124.70, 124.21, 117.23. **ESI-MS m/z** (100%), 420.3 ([M+H]$^+$).

N^2,N^6-di(quinolin-8-yl)pyridine-2,6-dicarboxamide (**1f**). The title compound was synthesized following the general synthetic procedure A, reacting pyridine-2,6-dicarbonyl-dichloride with 8-aminoquinoline with a final yield of 94%. **^{1}H NMR** ($CDCl_3$) δ 12.38 (s, 2H, NH), 9.04 (dd, J = 7.0, 2.0 Hz, 2H), 8.60 (d, J = 7.8 Hz, 2H), 8.28 (dd, J = 4.2, 1.7 Hz, 2H), 8.25 – 8.17 (m, 3H), 7.75 – 7.59 (m, 4H), 7.35 (dd, J = 8.2, 4.2 Hz, 2H). **^{13}C NMR** ($CDCl_3$) δ 162.01, 149.86, 148.70, 139.60, 139.34, 136.14, 134.42, 128.06, 127.37, 125.43, 122.35, 121.42, 117.28. **ESI-MS m/z** (100%), 420.3 ([M+H]$^+$).

N^2,N^6-di(isoquinolin-4-yl)pyridine-2,6-dicarboxamide (**1g**). The title compound was synthesized following the general synthetic procedure A, reacting pyridine-2,6-dicarbonyl-dichloride with 4-amino-isoquinoline with a final yield of 56%. **^{1}H NMR** (DMSO-d6) δ 11.46 (s, 2H, NH), 9.34 (s, 2H), 8.71 (s, 2H), 8.48 (d, J = 8.4 Hz, 2H), 8.38 (dd, J= 9.0,

Preprints (www.preprints.org) | NOT PEER-REVIEWED | Posted: 31 May 2021 doi:10.20944/preprints202105.0784.v1

6.5 Hz, 2H), 8.25 (d, J = 8.4 Hz, 2H), 8.11 (d, J = 8.4 Hz, 2H), 7.91 (td, J = 8.4, 1.3 Hz, 2H), 7.78 (td, J = 8.1, 1.2 Hz, 2H). **^{13}C NMR** (DMSO-d6) δ 163.45, 151.47, 148.85, 141.43, 140.73, 140.40, 132.45, 131.32, 128.98, 128.63, 128.35, 126.05, 123.08. **ESI-MS m/z** (100%), 420.3 ([M+H]$^+$).

N^2,N^6-di(isoquinolin-5-yl)pyridine-2,6-dicarboxamide (**1h**). The title compound was synthesized following the general synthetic procedure A, reacting pyridine-2,6-dicarbonyl-dichloride with 5-aminoisoquinoline with a final yield of %. **^{1}H NMR** (DMSO-d6) δ 11.46 (s, 2H, NH), 9.40 (d, J = 1.2 Hz, 2H), 8.60 (d, J = 6.0 Hz, 2H), 8.47 (d, J = 7.7 Hz, 2H), 8.38 (dd, J = 8.8, 6.5 Hz, 1H), 8.18 (d, J= 6 Hz, 2H), 7.99 (dd, J = 8.2, 1.2 Hz, 2H), 7.95 (d, J = 6.0 Hz, 2H), 7.80 (t, J = 8.2 Hz, 2H). **13C NMR** (DMSO-d6) δ 163.18, 153.09, 148.93, 143.52, 140.72, 132.74, 132.15, 129.25, 128.77, 127.77, 126.85, 126.00, 116.89. **ESI-MS m/z** (100%), 420.3 ([M+H]$^+$).

4.1.2 General procedure A for synthesis of bis-methyl-quinolinium/isoquinolinium-pyridine2,6-dicarboxamides (**2a-2d**).

In a round-bottom flask, 50 mg of pyridine-2,6-dicarboxamide (**1c**, **1e**, **1g** or **1h**, 0.119 mmol) were dissolved in 1.5 ml of a mixture DMF:Acetone (1:1). 148.5 µl of CH_3I were added to the reaction mixture, which was stirred for 5 days at room temperature. The resulting yellow precipitate was filtered and washed with cold MeOH to obtain the methylated bis-quinolinium/isoquinolinium iodide (**2a**-**2d**) with a yield of 50-60%.

3,3'-((pyridine-2,6-dicarbonyl)bis(azanediyl))bis(1- methylquinolin-1-ium) iodide (**2a**) 50 mg of **1c** (0.119 mmol) were dissolved in 1.5 ml of a mixture DMF/acetone (1:1). 148.5 µl of CH_3I were added to the mixture and stirred for 5 days at room temperature. The resulting yellow precipitate was filtered and washed with cold MeOH to give the title compound in 61 % yield. **^{1}H NMR** (DMSO-d6) δ 11.83 (s, 2H, NH), 10.13 (s, 2H), 9.67 (s, 2H), 8.62 – 8.53 (m, 6H), 8.49 (t, J = 7.7 Hz, 1H), 8.24 (t, J = 7.5 Hz, 2H), 8.08 (t, J = 7.6 Hz, 2H), 4.80 (s, 6H). **^{13}C NMR** (DMSO-d6) δ 162.5, 147.5, 144.7, 141.2, 135.9, 134.5, 134.1, 132.3, 130.5, 129.9, 129.3, 126.5, 122.8, 119.3, 118.5, 49.2. NMR data in agreement with previously reported in [40].). **ESI-MS m/z** 224.8 ([M-2I]$^{2+}$ (100%).

5,5' -((pyridine-2,6-dicarbonyl)bis(azanediyl))bis(2- methylisoquinolin-2-ium) iodide (**2b**) was obtained following the same conditions as 2a, using **1h** instead of 1c with a final yield of 56 %. **^{1}H NMR** (DMSO-d6) δ 11.65 (s, 2H, NH), 10.10 (s, 2H), 8.74 (d, J = 6.6 Hz, 2H), 8.65 (d, J = 6.9 Hz, 2H), 8.55 – 8.38 (m, 7H), 8.18 (t, J = 7.9 Hz, 2H), 4.52 (s, 6H). **^{13}C NMR** (DMSO-d6) δ 163.36, 151.61, 148.55, 141,11 (Detected via HMQC), 136.19, 134.22, 133.77, 133.34, 131.77, 129.33, 128.29, 126.40, 122.82, 48.46**. ESI-MS m/z** 224.8 ([M-2I]$^{2+}$, 100%); 448.3 ([M-H-2I]$^+$).

4,4'-((pyridine-2,6-dicarbonyl)bis(azanediyl))bis(1- methylquinolin-1-ium) iodide (**2c**) was obtained following the same conditions as 2a, using **1e** instead of 1c with a final 51 % yield. **^{1}H NMR** (DMSO-d6) δ 12.10 (s, 2H), 9.45 (d, J = 6.9 Hz, 2H), 9.11 (d, J = 8.5 Hz, 2H), 8.79 (d, J = 6.8 Hz, 2H), 8.68 (d, J = 7.7 Hz, 2H), 8.61 – 8.47 (m, 3H), 8.34 (t, J = 7.5 Hz, 2H), 8.08 (t, J = 7.7 Hz, 2H), 4.56 (s, 6H). **^{13}C NMR** (DMSO-d6) 163.84 (C=O), 150.73 (CH), 148.13 (C), 141.35 (CH), 139.95 (C), 135.76 (CH), 129.09 (CH), 128.19 (CH), 125.91 (CH), 125.60 (C), 121.96 (C), 119.98 (CH), 112.56 (CH), 45.16 (CH3). **ESI-MS m/z** 224.9 ([M-2I]$^{2+}$, 100%); 448.3 ([M-H-2I]$^+$).

4,4'-((pyridine-2,6-dicarbonyl)bis(azanediyl))bis(2- methylisoquinolin-2-ium) iodide (**2d**) was obtained following the same conditions as 2a, using **1g** instead of 1c, stirring for 2 days with a final 51% yield.

^{1}H NMR (DMSO-d6) δ 11.78 (s, 2H), 9.97 (s, 2H), 9.21 (s, 2H), 8.65 (d, J = 8.5 Hz, 2H), 8.58 (d, J = 7.6 Hz, 4H), 8.52 – 8.46 (m, 1H), 8.39 (t, J = 7.8 Hz, 2H), 8.17 (t, J = 7.7 Hz, 2H), 4.56 (s, 6H). **^{13}C NMR** (DMSO-d6) δ 163.34, 148.94, 148.17, 141.30 (Detected in HMQC), 136.99, 132.87, 132.84, 132.68, 132.09, 131.10, 128.04, 127.06, 123.94, 48.95. **ESI-MS m/z** 224.8 ([M-2I]$^{2+}$, 100%); 448.3 ([M-H-2I]$^+$).

Preprints (www.preprints.org) | NOT PEER-REVIEWED | Posted: 31 May 2021 doi:10.20944/preprints202105.0784.v1

4.2 PCR-Stop assay

The protocol for PCR-Stop assay and the primer design was adapted from a previously reported protocol [46]. For the complete sequence list, refer to Table S3 (supplementary material). Briefly, for each reaction, 0.5μL of Taq DNA Polymerase, 2.0 μL of Termopol buffer, 1.0 μL of dNTP mix, 1.0 μL of each primer (straight + reverse, 25μM) solutions were added, for a total volume of 5.5μL. The calculated volume of tested compound is added to the required final concentration, for a final volume of 20μL (Physiological solution was added to reach this final volume). The tubes so prepared, were placed on a thermo-cycler with the following cycling conditions: 94 °C for 3 min, followed by 10 cycles of 94 °C for 30 s, 58 °C for 30 s, and 72 °C for 30 s. After the amplification, 2 μl of stop solution (marked with bromophenol blue) were added. The amplified products were separated running electrophoresis in 10% polyacrylamide gel (PAGE). The gel was stained with ethidium bromide and photographed under UV light.

4.3. FRET-Melting analysis and competition experiments

Working solutions of 5'-FAM/3'TAMRA- labelled oligonucleotides (please refer to table **S1** for the complete sequence list) were freshly prepared, diluted with FRET buffer (60 mM KCl, potassium cacodylate pH 7.4) at a final concentration of 20 μM. These were diluted at 0.4 μM and annealed at 95°C for 10 minutes in a heating block, then slowly cooled to room temp. (over 1.5 h). 50 μL of annealed DNA solution were mixed with 50 μL of tested compound at the appropriate concentration, in 96-Well RT-PCR plates, with a final DNA concentration of 0.2 μM. Fluorescence readings were taken at intervals of 0.5 °C, in the range 31–95 °C. The advanced curve-fitting function in GraphPad Prism (nonlinear regression fit) was used for calculation of ΔTm values. Only results with fitting r^2 values > 0.75 were considered.

For the competition experiments, the melting of the k-RAS G4 (0.2 μM) complexed with ligand (5 μM or 0.5 μM) was monitored under the same conditions, including 0.4, 2.0, 10, and 25 μM of non-fluorescent double-stranded competitor 26ds DNA, using the same FRET assay conditions.

4.4 CD titration and melting analyses

All CD measurements were performed at 20 °C at 10 μM strand concentration of oligonucleotide in 20 mM lithium cacodylate containing 10 mM KCl and 90 mM LiCl for *h-Telo,* 20 mM lithium cacodylate containing 100 mM LiCl for *c-MYC* and 20 mM lithium cacodylate containing 50 mM KCl for *k-RAS*. The sequences were annealed by heating to 95 °C for 10 min followed by cooling on ice for 1 h. For CD titration experiments, a 10 mM stock solution of each ligand was prepared in DMSO and the required volume for each point was added directly to a 1 mm quartz cell containing the oligonucleotide solution. CD spectra were recorded using a Jasco J-815 spectrapolarimeter equipped with a Peltier-type temperature control system (model CDF-426S/15), using an instrument scanning speed of 200 nm/min with a response time of 1 s in wavelengths ranging from 200 to 340 nm. The recording bandwidth was 1 nm with 1 nm step size. The spectra were signal averaged over four scans and baseline corrected by subtracting a buffer spectrum.

CD melting spectra were acquired in the temperature range 20-100 °C, with a heating rate of 1 °C/min by monitoring the ellipticity at 290 and 265 nm for telomeric DNA and oncogene promoters, respectively. Spectra were acquired in the presence of 1, 5 and 10 molar equivalents of ligand. CD melting spectra were acquired in in 20 mM potassium phosphate buffer containing 10 mM KCl. Data was converted into fraction folded plots, fit to a Boltzmann distribution and the melting temperatures determined from the two-state transition model (OriginPro 8).

4.5 Molecular modeling

 doi:10.20944/preprints202105.0784.v1

4.5.1. Compound structure preparation

The 3D structures of **2a, 2b, 2c** and **2d** compounds were initially generated using the MarvinSketch (version 20.13) software from Chemaxon (http:www.chemaxon.com). The resulting geometries were then optimized at the B3LYP/6-31G(d) level of theory [49–53], using Gaussian 09, Rev A.2 [54]. To derive the partial atomic charges for each compound, we have used the strategy described for GAFF [51,55], with the molecular electrostatic potentials (ESP) created for all elements at the HF/6-31G(d) [56–58] level of theory. The overall charge of each compound was set to +2. The atomic partial charges were afterwards derived following the restrained ESP (RESP) [59] procedure, using the antechamber [60] module implemented in AmberTools19 [61].

4.5.2. Molecular dynamics simulations

All molecular mechanics/dynamics (MM/MD) simulations were performed using the GROMACS 2018.6 software package [62–64] as well as the OL15 refinement of the Amber14sb force field [65–68].

The initial structure of the k-RAS molecule was taken from PDB 5i2v [69]. Four different systems were built, each consisting of the quadruplex and one of the four compounds previously parameterized. Amber topologies were built for each compound using the tleap module in AmberTools19 [61], which were subsequently converted to GROMACS format using ACPYPE [70]. Five different replicate simulations were built for each system. In each replicate, one copy of each compound was manually placed in different positions around k-RAS. These systems were then initially solvated using TIP3P water molecules [71,72] in a dodecahedric box, and the overall system charge was neutralized by randomly replacing 17 water molecules with K+ ions, via the gmx genion tool. Next, the systems underwent a 2-step energy minimization procedure using the steepest descent algorithm [73]: first, with no constraints, and second with hydrogen bond constraints. Velocities were then generated according to a Maxwell distribution at 298.15 K.

Each replicate was then simulated for 750 ns, using the particle mesh Ewald (PME) method to treat long-range electrostatic interactions [74,75] with a Fourier grid spacing of 0.12 nm and a cutoff of 1.4 nm for direct contributions. Lennard-Jones interactions were calculated using a neighbor pair list with a cutoff of 1.4 nm and using a Verlet scheme [76]. Solute bonds were constrained using the parallel linear constraint solver P-LINCS [77], while water molecules were constrained using the SETTLE algorithm [78]. The temperature was kept at 298.15 K using a Nosé-Hoover thermostat [79,80] with a coupling constant of 1 ps, and an isotropic Parrinello-Rahman barostat [81,82] was used to keep the pressure constant at 1 bar with a coupling constant of 5 ps and a compressibility of 4.5 x 10-5 bar-1.

Analyses were performed using several GROMACS tools. In addition, plots were made using Gnuplot [83] and all 3D conformations were built using PyMOL [84].

4.5.3. MM/PBSA calculations

To calculate the binding free energies of the different compounds to the k-RAS, we have used the program g_mmpbsa developed by Kumari et al. [85,86]. Analogously to other studies [87], we have used a single trajectory approach, which assumes the quadruplex and the ligand conformation in the bound and unbound states to be identical. Equations used to determine binding free energies can be found in Supporting Information.

Supplementary Materials: The following are available online at www.mdpi.com/xxx/s1, Figure S1. CD titration of c-MYC in presence of increasing equivalents (0-25) of compound 2a (A), 2b (B), 2c (C), 2d (D); Figure S2. CD titration of k-RAS in presence of increasing equivalents (0-25) of compound 2a (A), 2b (B), 2c (C), 2d (D); Figure S3. A) Results of PCR-stop assay of compounds 1a-eat 50 for c-MYC gene promoter Pu27. B) Results of PCR-stop assay of compound 2a for c-MYC gene promoter Pu27 and for mutated c-MYC gene promoter (Pu27mut); Figure S4. Root mean square

deviation (RMSD) of the complex k-RAS + ligand, throughout the simulation time for each replicate simulation; Figure S5. Variation of the MM/PBSA binding free energy between the different ligands and k-RAS for each replicate simulation; Figure S6. Minimum distance of compound 2a to each pair of bases of k-RAS for all replicate simulations; Figure S7. Minimum distance of compound 2b to each pair of bases of k-RAS for all replicate simulations; Figure S8. Minimum distance of compound 2c to each pair of bases of k-RAS for all replicate simulations; Figure S9. Minimum distance of compound 2d to each pair of bases of k-RAS for all replicate simulations. Figure S10-S19 NMR characterization of the synthesized molecules; Table S1. Sequences used in FRET-melting experiments; Table S2. Sequences used in CD experiments; Table S3. Sequences used in PCR-stop assay

Author Contributions:

Conceptualization of the study, A.P.; Synthesis, E.C. and A.P.; FRET-melting experiments, E.C. and E.M.; CD experiments, J.C. and C.C.; PCR-stop assay, E.C. and J.B.V.; Molecular modeling, P.R.M., R.M.E. and B.L.V.; writing—review and editing, all authors. All authors have read and agreed to the published version of the manuscript.

Funding: This research was funded by European Structural & Investment Funds through the COMPETE Program—Programa Operacional de Lisboa under Program grant LISBOA-01-0145-FEDER-016405, and from Fundação para a Ciência e Tecnologia (FCT, Portugal), project grant SAICT-PAC/0019/2015, UIDP/04138/2020 of iMed, UIDB/00709/2020 of CICS, PTDC/BIA-BFS/28419/2017, strategic project UIDB/04046/2020-UIDP/04046/2020 (BioISI) and project ref. IF/00959/2015 funded by Fundo Social Europeu e Programa Operacional Potencial Humano. J.B.V.'s research group was financed by New England Biolabs, Inc. (USA).

Acknowledgments: We thank Paulo J. Costa for fruitful discussions in the parameterization of the ligands for the molecular modeling studies; Portuguese Mass Spectrometry National Network for the LC-MS service. E.C. acknowledges Prof. Dr. Rui Moreira for having accepted him in iMed group to work in this project, within the context of Erasmus+ programme.

Conflicts of Interest: The authors declare no conflict of interest.

References

1. Sung, H.; Ferlay, J.; Siegel, R.L.; Laversanne, M.; Soerjomataram, I.; Jemal, A.; Bray, F. Global cancer statistics 2020: GLOBOCAN estimates of incidence and mortality worldwide for 36 cancers in 185 countries. *CA. Cancer J. Clin.* **2021**, *0*, 1–41, doi:10.3322/caac.21660.

2. Nesbit, C.E.; Tersak, J.M.; Prochownik, E. V. MYC oncogenes and human neoplastic disease. *Oncogene* **1999**, *18*, 3004–3016, doi:10.1038/sj.onc.1202746.

3. Boxer, L.M.; Dang, C. V. Translocations involving c-myc and c-myc function. *Oncogene* **2001**, *20*, 5595–5610, doi:10.1038/sj.onc.1204595.

4. Fernandez-Medarde, A.; Santos, E. Ras in Cancer and Developmental Diseases. *Genes Cancer* **2011**, *2*, 344–358, doi:10.1177/1947601911411084.

5. Adjei, A.A. Blocking oncogenic Ras signaling for cancer therapy. *J Natl.Cancer Inst.* **2001**, *93*, 1062–1074, doi:10.1016/S0378-4274(02)00422-8.

6. Saleem, M.; Babaei, A.; Press, D. Receptor tyrosine kinase (c-Kit) inhibitors : a potential therapeutic target in cancer cells. **2016**, 2443–2459, doi:10.2147/DDDT.S89114.

7. Gustafson, W.C.; Weiss, W.A. Myc proteins as therapeutic targets. *Oncogene* **2010**, *29*, 1249–1259, doi:10.1038/onc.2009.512.

8. McCormick, F. KRAS as a therapeutic target. *Clin. Cancer Res.* **2015**, *21*, 1797–1801, doi:10.1158/1078-0432.CCR-14-2662.

9. Phan, A.T.; Kuryavyi, V.; Burge, S.; Neidle, S.; Patel, D.J. Structure of an unprecedented G-quadruplex scaffold in the human c-kit promoter. *J. Am. Chem. Soc.* **2007**, *129*, 4386–4392, doi:10.1021/ja068739h.

10. Cogoi, S.; Xodo, L.E. G-quadruplex formation within the promoter of the KRAS proto-oncogene and its effect on transcription. *Nucleic Acids Res.* **2006**, *34*, 2536–2549, doi:10.1093/nar/gkl286.

11. Cogoi, S.; Paramasivam, M.; Spolaore, B.; Xodo, L.E. Structural polymorphism within a regulatory element of the human KRAS promoter: Formation of G4-DNA recognized by nuclear proteins. *Nucleic Acids Res.* **2008**, *36*, 3765–3780, doi:10.1093/nar/gkn120.

12. Siddiqui-Jain, A.; Grand, C.L.; Bearss, D.J.; Hurley, L.H. Direct evidence for a G-quadruplex in a promoter region and its targeting with a small molecule to repress c-MYC transcription. *Proc. Natl. Acad. Sci.* **2002**, *99*, 11593–11598, doi:10.1073/pnas.182256799.

13. Largy, E.; Mergny, J.-L.; Gabelica, V. Role of Alkali Metal Ions in G-Quadruplex Nucleic Acid Structure and Stability. In; Sigel, A., Sigel, H., Sigel, R.K.O., Eds.; Metal Ions in Life Sciences; Springer International Publishing: Cham, 2016; Vol. 16, pp. 203–258 ISBN 978-3-319-21755-0.

14. Phan, A.T.; Mergny, J.-L. Human telomeric DNA: G-quadruplex, i-motif and Watson-Crick double helix. *Nucleic Acids Res.* **2002**, *30*, 4618–4625, doi:10.1093/nar/gkf597.

15. Pennarun, G.; Granotier, C.; Gauthier, L.R.; Gomez, D.; Hoffschir, F.; Mandine, E.; Riou, J.-F.; Mergny, J.; Mailliet, P.; Boussin, F.D. Apoptosis related to telomere instability and cell cycle alterations in human glioma cells treated by new highly selective G-quadruplex ligands. *Oncogene* **2005**, *24*, 2917–2928, doi:10.1038/sj.onc.1208468.

16. Greider, C.W. Telomere length regulation. *Annu. Rev. Biochem.* **1996**, *65*, 337–365, doi:10.1146/annurev.bi.65.070196.002005.

17. Murat, P.; Balasubramanian, S. Existence and consequences of G-quadruplex structures in DNA. *Curr. Opin. Genet. Dev.* **2014**, *25*, 22–29, doi:10.1016/j.gde.2013.10.012.

18. Hänsel-hertsch, R.; Beraldi, D.; Lensing, S. V; Marsico, G.; Zyner, K.; Parry, A.; Antonio, M. Di; Pike, J.; Kimura, H.; Narita, M.; et al. G-quadruplex structures mark human regulatory chromatin. *Nat. Genet.* **2016**, *48*, 1267–1272, doi:10.1038/ng.3662.

19. Hänsel-Hertsch, R.; Di Antonio, M.; Balasubramanian, S. DNA G-quadruplexes in the human genome: detection, functions and therapeutic potential. *Nat. Rev. Mol. Cell Biol.* **2017**, *18*, 279–284, doi:10.1038/nrm.2017.3.

20. Varshney, D.; Spiegel, J.; Zyner, K.; Tannahill, D.; Balasubramanian, S. The regulation and functions of DNA and RNA G-quadruplexes. *Nat. Rev. Mol. Cell Biol.* **2020**, *21*, 459–474, doi:10.1038/s41580-020-0236-x.

21. Cadoni, E.; De Paepe, L.; Manicardi, A.; Madder, A. Beyond small molecules: targeting G-quadruplex structures with oligonucleotides and their analogues. *Nucleic Acids Res.* **2021**, 1–22, doi:10.1093/nar/gkab334.

22. Neidle, S. Quadruplex Nucleic Acids as Novel Therapeutic Targets. *J. Med. Chem.* **2016**, *59*, 5987–6011, doi:10.1021/acs.jmedchem.5b01835.

23. Paulo, A.; Castillo, C.C.; Neidle, S. Targeting Promoter Quadruplex Nucleic Acids for Cancer Therapy. In *Comprehensive Medicinal Chemistry III*; Elsevier, 2017; Vol. 5, pp. 308–340 ISBN 9780124095472.

24. Duarte, A.R.; Cadoni, E.; Ressurreição, A.S.; Moreira, R.; Paulo, A. Design of Modular G-quadruplex Ligands. *ChemMedChem* **2018**, *13*, 869–893, doi:10.1002/cmdc.201700747.

25. Carvalho, J.; Mergny, J.L.; Salgado, G.F.; Queiroz, J.A.; Cruz, C. G-quadruplex, Friend or Foe: The Role of the G-quartet in Anticancer Strategies. *Trends Mol. Med.* **2020**, *26*, 848–861, doi:10.1016/j.molmed.2020.05.002.

26. Summers, P.A.; Lewis, B.W.; Gonzalez-Garcia, J.; Porreca, R.M.; Lim, A.H.M.; Cadinu, P.; Martin-Pintado, N.; Mann, D.J.; Edel, J.B.; Vannier, J.B.; et al. Visualising G-quadruplex DNA dynamics in live cells by fluorescence lifetime imaging microscopy. *Nat. Commun.* **2021**, *12*, 1–11, doi:10.1038/s41467-020-20414-7.

27. Biffi, G.; Tannahill, D.; McCafferty, J.; Balasubramanian, S. Quantitative visualization of DNA G-quadruplex structures in human cells. *Nat. Chem.* **2013**, *5*, 182–186, doi:10.1038/nchem.1548.

28. Biffi, G.; Di Antonio, M.; Tannahill, D.; Balasubramanian, S. Visualization and selective chemical targeting of RNA G-quadruplex structures in the cytoplasm of human cells. *Nat. Chem.* **2014**, *6*, 75–80, doi:10.1038/nchem.1805.

29. Pennarun, G.; Granotier, C.; Gauthier, L.R.; Gomez, D.; Hoffschir, F.; Mandine, E.; Riou, J.F.; Mergny, J.L.; Mailliet, P.; Boussin, F.D. Apoptosis related to telomere instability and cell cycle alterations in human glioma cells treated by new highly selective G-quadruplex ligands. *Oncogene* **2005**, *24*, 2917–2928, doi:10.1038/sj.onc.1208468.

30. De Cian, A.; DeLemos, E.; Mergny, J.-L.; Teulade-Fichou, M.-P.; Monchaud, D. Highly Efficient G-Quadruplex Recognition by Bisquinolinium Compounds. *J. Am. Chem. Soc.* **2007**, *129*, 1856–1857, doi:10.1021/ja067352b.

31. Dhamodharan, V.; Harikrishna, S.; Jagadeeswaran, C.; Halder, K.; Pradeepkumar, P.I. Selective G-quadruplex DNA Stabilizing Agents Based on Bisquinolinium and Bispyridinium Derivatives of 1,8-Naphthyridine. **2012**.

32. Peng, D.; Tan, J.H.; Chen, S. Bin; Ou, T.M.; Gu, L.Q.; Huang, Z.S. Bisaryldiketene derivatives: A new class of selective ligands for c-myc G-quadruplex DNA. *Bioorganic Med. Chem.* **2010**, *18*, 8235–8242, doi:10.1016/j.bmc.2010.10.021.

33. Granotier, C.; Pennarun, G.; Riou, L.; Hoffschir, F.; Gauthier, L.R.; De Cian, A.; Gomez, D.; Mandine, E.; Riou, J.F.; Mergny, J.L.; et al. Preferential binding of a G-quadruplex ligand to human chromosome ends. *Nucleic Acids Res.* **2005**, *33*, 4182–4190, doi:10.1093/nar/gki722.

34. Verga, D.; Hamon, F.; Poyer, F.; Bombard, S.; Teulade-Fichou, M.P. Photo-cross-linking probes for trapping G-quadruplex DNA. *Angew. Chemie - Int. Ed.* **2014**, *53*, 994–998, doi:10.1002/anie.201307413.

35. Cadoni, E.; Manicardi, A.; Fossépré, M.; Heirwegh, K.; Surin, M.; Madder, A. Teaching photosensitizers a new

trick: red light-triggered G-quadruplex alkylation by ligand co-localization. *Chem. Commun.* **2021**, *57*, 1010–1013, doi:10.1039/d0cc06030e.

36. Su, H.; Xu, J.; Chen, Y.; Wang, Q.; Lu, Z.; Chen, Y.; Chen, K.; Han, S.; Fang, Z.; Wang, P.; et al. Photoactive G-Quadruplex Ligand Identifies Multiple G-Quadruplex-Related Proteins with Extensive Sequence Tolerance in the Cellular Environment. *J. Am. Chem. Soc.* **2021**, *143*, 1917–1923, doi:10.1021/jacs.0c10792.

37. Yang, P.; De Cian, A.; Teulade-Fichou, M.P.; Mergny, J.L.; Monchaud, D. Engineering bisquinolinium/thiazole orange conjugates for fluorescent sensing of G-quadruplex DNA. *Angew. Chemie - Int. Ed.* **2009**, *48*, 2188–2191, doi:10.1002/anie.200805613.

38. Monchaud, D.; Yang, P.; Lacroix, L.; Teulade-Fichou, M.P.; Mergny, J.L. A metal-mediated conformational switch controls G-quadruplex binding affinity. *Angew. Chemie - Int. Ed.* **2008**, *47*, 4858–4861, doi:10.1002/anie.200800468.

39. Marchand, A.; Granzhan, A.; Iida, K.; Tsushima, Y.; Ma, Y.; Nagasawa, K.; Teulade-Fichou, M.P.; Gabelica, V. Ligand-induced conformational changes with cation ejection upon binding to human telomeric DNA G-quadruplexes. *J. Am. Chem. Soc.* **2015**, *137*, 750–756, doi:10.1021/ja5099403.

40. Dorazco-González, A.; Höpfl, H.; Medrano, F.; Yatsimirsky, A.K. Recognition of anions and neutral guests by dicationic pyridine-2,6- dicarboxamide receptors. *J. Org. Chem.* **2010**, *75*, 2259–2273, doi:10.1021/jo100037m.

41. Dorazco-González, A.; Alamo, M.F.; Godoy-Alcántar, C.; Höpfl, H.; Yatsimirsky, A.K. Fluorescent anion sensing by bisquinolinium pyridine-2,6-dicarboxamide receptors in water. *RSC Adv.* **2014**, *4*, 455–466, doi:10.1039/C3RA44363A.

42. Gray, R.D.; Petraccone, L.; Trent, J.O.; Chaires, J.B. Characterization of a K+-induced conformational switch in a human telomeric DNA oligonucleotide using 2-aminopurine fluorescence. *Biochemistry* **2010**, *49*, 179–194, doi:10.1021/bi901357r.

43. Dai, J.; Carver, M.; Punchihewa, C.; Jones, R.A.; Yang, D. Structure of the hybrid-2 type intramolecular human telomeric G-quadruplex in K+ solution: Insights into structure polymorphism of the human telomeric sequence. *Nucleic Acids Res.* **2007**, *35*, 4927–4940, doi:10.1093/nar/gkm522.

44. Ambrus, A.; Chen, D.; Dai, J.; Bialis, T.; Jones, R.A.; Yang, D. Human telomeric sequence forms a hybrid-type intramolecular G-quadruplex structure with mixed parallel/antiparallel strands in potassium solution. *Nucleic Acids Res.* **2006**, *34*, 2723–2735, doi:10.1093/nar/gkl348.

45. Ambrus, A.; Chen, D.; Dai, J.; Jones, R.A.; Yang, D. Solution structure of the biologically relevant G-quadruplex element in the human c-MYC promoter. Implications for G-quadruplex stabilization. *Biochemistry* **2005**, *44*, 2048–2058, doi:10.1021/bi048242p.

46. Mendes, E.; Cadoni, E.; Carneiro, F.; Afonso, M.B.; Brito, H.; Lavrado, J.; dos Santos, D.J.V.A.; Vítor, J.B.; Neidle, S.; Rodrigues, C.M.P.; et al. Combining 1,3-ditriazolyl-benzene and quinoline to discover a new G-quadruplex interactive small molecule active against cancer stem-like cells. *ChemMedChem* **2019**, cmdc.201900243, doi:10.1002/cmdc.201900243.

47. Lemarteleur, T.; Gomez, D.; Paterski, R.; Mandine, E.; Mailliet, P.; Riou, J.F. Stabilization of the c-myc gene promoter quadruplex by specific ligands' inhibitors of telomerase. *Biochem. Biophys. Res. Commun.* **2004**, *323*, 802–808, doi:10.1016/j.bbrc.2004.08.150.

48. Müller, S.; Sanders, D.A.; Di Antonio, M.; Matsis, S.; Riou, J.-F.; Rodriguez, R.; Balasubramanian, S. Pyridostatin analogues promote telomere dysfunction and long-term growth inhibition in human cancer cells. *Org. Biomol. Chem.* **2012**, *10*, 6537, doi:10.1039/c2ob25830g.

49. Krishnan, R.; Binkley, J.S.; Seeger, R.; Pople, J.A. Self-consistent molecular orbital methods. XX. A basis set for correlated wave functions. *J. Chem. Phys.* **1980**, *72*, 650–654, doi:10.1063/1.438955.

50. McLean, A.D.; Chandler, G.S. Contracted Gaussian basis sets for molecular calculations. I. Second row atoms, Z =11–18. *J. Chem. Phys.* **1980**, *72*, 5639–5648, doi:10.1063/1.438980.

51. Becke, A.D. Density-functional exchange-energy approximation with correct asymptotic behavior. *Phys. Rev. A* **1988**, *38*, 3098–3100, doi:10.1103/PhysRevA.38.3098.

52. Lee, C.; Yang, W.; Parr, R.G. Development of the Colle-Salvetti correlation-energy formula into a functional of the electron density. *Phys. Rev. B* **1988**, *37*, 785–789, doi:10.1103/PhysRevB.37.785.

53. Curtiss, L.A.; McGrath, M.P.; Blaudeau, J.; Davis, N.E.; Binning, R.C.; Radom, L. Extension of Gaussian-2 theory to molecules containing third-row atoms Ga–Kr. *J. Chem. Phys.* **1995**, *103*, 6104–6113, doi:10.1063/1.470438.

54. Frisch, M.J.; Trucks, G.W.; Schlegel, H.B.; Scuseria, G.E.; Robb, M.A.; Cheeseman, J.R.; Scalmani, G.; Barone, V.; Mennucci, B.; Petersson, G.A.Frisch, M.J.; Trucks, G.W.; Schlegel, H.B.; Scuseria, G.E.; Robb, M.A.; Cheeseman, J.R.; Scalmani, G.; Barone, G.A. Gaussian 09, Revision A.2 2009.

55. Wang, J.; Wolf, R.M.; Caldwell, J.W.; Kollman, P.A.; Case, D.A. Development and testing of a general amber force field. *J. Comput. Chem.* **2004**, *25*, 1157–1174, doi:10.1002/jcc.20035.

56. Hariharan, P.C.; Pople, J.A. The influence of polarization functions on molecular orbital hydrogenation energies. *Theor. Chim. Acta* **1973**, *28*, 213–222, doi:10.1007/BF00533485.

57. Francl, M.M.; Pietro, W.J.; Hehre, W.J.; Binkley, J.S.; Gordon, M.S.; DeFrees, D.J.; Pople, J.A. Self-consistent molecular orbital methods. XXIII. A polarization-type basis set for second-row elements. *J. Chem. Phys.* **1982**, *77*, 3654–3665, doi:10.1063/1.444267.

58. Rassolov, V.A.; Ratner, M.A.; Pople, J.A.; Redfern, P.C.; Curtiss, L.A. 6-31G* basis set for third-row atoms. *J. Comput. Chem.* **2001**, *22*, 976–984, doi:10.1002/jcc.1058.

59. Bayly, C.I.; Cieplak, P.; Cornell, W.; Kollman, P.A. A well-behaved electrostatic potential based method using charge restraints for deriving atomic charges: the RESP model. *J. Phys. Chem.* **1993**, *97*, 10269–10280, doi:10.1021/j100142a004.

60. Wang, J.; Wang, W.; Kollman, P.A.; Case, D.A. Automatic atom type and bond type perception in molecular mechanical calculations. *J. Mol. Graph. Model.* **2006**, *25*, 247–260, doi:10.1016/j.jmgm.2005.12.005.

61. Case, D.A.; Cerutti, D.S.; Cheatham, T.E., III; Darden, T.A.; Duke, R.E.; Giese, T.J.; Gohlke, H.; Goetz, A.W.; Greene, D.; Homeyer, N. AMBER 2019 2019.

62. Berendsen, H.J.C.; van der Spoel, D.; van Drunen, R. GROMACS: A message-passing parallel molecular dynamics implementation. *Comput. Phys. Commun.* **1995**, *91*, 43–56, doi:10.1016/0010-4655(95)00042-E.

63. Van Der Spoel, D.; Lindahl, E.; Hess, B.; Groenhof, G.; Mark, A.E.; Berendsen, H.J.C. GROMACS: Fast, flexible, and free. *J. Comput. Chem.* **2005**, *26*, 1701–1718, doi:10.1002/jcc.20291.

64. Abraham, M.J.; Murtola, T.; Schulz, R.; Páll, S.; Smith, J.C.; Hess, B.; Lindahl, E. GROMACS: High performance molecular simulations through multi-level parallelism from laptops to supercomputers. *SoftwareX* **2015**, *1–2*, 19–25, doi:10.1016/j.softx.2015.06.001.

65. Zgarbová, M.; Otyepka, M.; Šponer, J.; Mládek, A.; Banáš, P.; Cheatham, T.E.; Jurečka, P. Refinement of the Cornell et al. Nucleic Acids Force Field Based on Reference Quantum Chemical Calculations of Glycosidic Torsion Profiles. *J. Chem. Theory Comput.* **2011**, *7*, 2886–2902, doi:10.1021/ct200162x.

66. Zgarbová, M.; Šponer, J.; Otyepka, M.; Cheatham, T.E.; Galindo-Murillo, R.; Jurečka, P. Refinement of the Sugar–Phosphate Backbone Torsion Beta for AMBER Force Fields Improves the Description of Z- and B-DNA. *J. Chem. Theory Comput.* **2015**, *11*, 5723–5736, doi:10.1021/acs.jctc.5b00716.

67. Maier, J.A.; Martinez, C.; Kasavajhala, K.; Wickstrom, L.; Hauser, K.E.; Simmerling, C. ff14SB: Improving the Accuracy of Protein Side Chain and Backbone Parameters from ff99SB. *J. Chem. Theory Comput.* **2015**, *11*, 3696–3713, doi:10.1021/acs.jctc.5b00255.

68. Allnér, O.; Nilsson, L.; Villa, A. Magnesium Ion–Water Coordination and Exchange in Biomolecular Simulations. *J. Chem. Theory Comput.* **2012**, *8*, 1493–1502, doi:10.1021/ct3000734.

69. Kerkour, A.; Marquevielle, J.; Ivashchenko, S.; Yatsunyk, L.A.; Mergny, J.-L.; Salgado, G.F. High-resolution three-dimensional NMR structure of the KRAS proto-oncogene promoter reveals key features of a G-quadruplex involved in transcriptional regulation. *J. Biol. Chem.* **2017**, *292*, 8082–8091, doi:10.1074/jbc.M117.781906.

70. Sousa da Silva, A.W.; Vranken, W.F. ACPYPE - AnteChamber PYthon Parser interfacE. *BMC Res. Notes* **2012**, *5*, 367, doi:10.1186/1756-0500-5-367.

71. Jorgensen, W.L.; Chandrasekhar, J.; Madura, J.D.; Impey, R.W.; Klein, M.L. Comparison of simple potential functions for simulating liquid water. *J. Chem. Phys.* **1983**, *79*, 926–935, doi:10.1063/1.445869.

72. Neria, E.; Fischer, S.; Karplus, M. Simulation of activation free energies in molecular systems. *J. Chem. Phys.* **1996**, *105*, 1902–1921, doi:10.1063/1.472061.

73. Luenberger, D.G.; Ye, Y. Linear and Nonlinear Programming. In *Vol 228*; 2008; pp. 213–262 ISBN 978-3-319-18841-6.

74. Darden, T.; York, D.; Pedersen, L. Particle mesh Ewald: An N ·log(N) method for Ewald sums in large systems. *J. Chem. Phys.* **1993**, *98*, 10089–10092, doi:10.1063/1.464397.

75. Essmann, U.; Perera, L.; Berkowitz, M.L.; Darden, T.; Lee, H.; Pedersen, L.G. A smooth particle mesh Ewald method. *J. Chem. Phys.* **1995**, *103*, 8577–8593, doi:10.1063/1.470117.

76. Páll, S.; Hess, B. A flexible algorithm for calculating pair interactions on SIMD architectures. *Comput. Phys. Commun.* **2013**, *184*, 2641–2650, doi:10.1016/j.cpc.2013.06.003.

77. Hess, B. P-LINCS: A Parallel Linear Constraint Solver for Molecular Simulation. *J. Chem. Theory Comput.* **2008**, *4*, 116–122, doi:10.1021/ct700200b.

78. Miyamoto, S.; Kollman, P.A. Settle: An analytical version of the SHAKE and RATTLE algorithm for rigid water models. *J. Comput. Chem.* **1992**, *13*, 952–962, doi:10.1002/jcc.540130805.

79. Nosé, S. A unified formulation of the constant temperature molecular dynamics methods. *J. Chem. Phys.* **1984**, *81*, 511–519, doi:10.1063/1.447334.

80. Hoover, W.G. Canonical dynamics: Equilibrium phase-space distributions. *Phys. Rev. A* **1985**, *31*, 1695–1697, doi:10.1103/PhysRevA.31.1695.

81. Nosé, S.; Klein, M.L. Constant pressure molecular dynamics for molecular systems. *Mol. Phys.* **1983**, *50*, 1055–1076, doi:10.1080/00268978300102851.

82. Parrinello, M.; Rahman, A. Polymorphic transitions in single crystals: A new molecular dynamics method. *J. Appl. Phys.* **1981**, *52*, 7182–7190, doi:10.1063/1.328693.

83. Williams, T.; Kelley, C.; Bersch, C. Gnuplot 5.2 an interactive plotting program 2019.

84. DeLano, W.L. The Pymol Molecular Graphics System 2003.

85. Kumari, R.; Kumar, R.; Lynn, A. g_mmpbsa —A GROMACS Tool for High-Throughput MM-PBSA Calculations. *J. Chem. Inf. Model.* **2014**, *54*, 1951–1962, doi:10.1021/ci500020m.

86. Baker, N.A.; Sept, D.; Joseph, S.; Holst, M.J.; McCammon, J.A. Electrostatics of nanosystems: Application to microtubules and the ribosome. *Proc. Natl. Acad. Sci.* **2001**, *98*, 10037–10041, doi:10.1073/pnas.181342398.

87. Rizzo, R.C.; Aynechi, T.; Case, D.A.; Kuntz, I.D. Estimation of Absolute Free Energies of Hydration Using Continuum Methods: Accuracy of Partial Charge Models and Optimization of Nonpolar Contributions. *J. Chem. Theory Comput.* **2006**, *2*, 128–139, doi:10.1021/ct050097l.